UVIT Survey of the Host Galaxies of Active Galactic Nuclei. I. Star Formation Scenarios

Payel Nandi[1,2] , C. S. Stalin[2] , Poulomi Dam[2,3] , and D. J. Saikia[4]

[1] Joint Astronomy Programme, Department of Physics, Indian Institute of Science, Bangalore 560012, India; payel.nandi@iiap.res.in
[2] Indian Institute of Astrophysics, Block II, Koramangala, Bangalore 560034, India
[3] Dipartimento di Fisica e Astronomia, Università di Padova, Vicolo dell'Osservatorio 3, I-35122 Padova, Italy
[4] Inter-University Centre for Astronomy and Astrophysics, Pune 411007, India

Abstract

Circumnuclear star formation (SF) is generally seen in galaxies hosting active galactic nuclei (AGN); however, the connection between the AGN activity and SF in them is less well understood. To explore this connection on scales of a few tens of parsecs to a few tens of kiloparsecs and larger, we carried out an investigation of SF in seven Seyfert-type AGN and one low-ionization nuclear emission-line region galaxy, using observations with the Ultraviolet Imaging Telescope on board AstroSat in the near-ultraviolet (2000–3000 Å) and far-ultraviolet (1300 −1800 Å) bands. A total of 1742 star-forming regions were identified, having size scales of 0.010–63.642 kpc². Considering all the galaxies, we found a positive correlation between their total surface density of SF (Σ_{SFR}) and extinction. For five galaxies, namely NGC 1365, NGC 4051, NGC 4321, NGC 5033, and NGC 6814, we found a gradual decrease of both extinction and Σ_{SFR} from the centre to the outer regions. Four sources are found to lie in the main sequence of star-forming galaxies, and the other four lie away from it. We found the ratio of the star formation rate (SFR) in the nuclear region to the total SFR to be positively correlated with the Eddington ratio. This points to the influence of AGN in enhancing the SF characteristics of the hosts. However, the impact is dominant only in the central nuclear region and has no significant effect on the larger scales probed in this work.

Materials only available in the online version of record: machine-readable table

1. Introduction

The observational evidence of close correlation between the mass of the supermassive black holes that power active galactic nuclei (AGN) via accretion and their host galaxy properties (Ferrarese & Merritt 2000; Gebhardt et al. 2000; McLure & Dunlop 2002; Marconi & Hunt 2003; Häring & Rix 2004) clearly indicates that AGN and star formation (SF) are closely linked. This connection is believed to be via AGN feedback processes, which play an important role in the SF characteristics of their hosts from the central nuclear scales to larger galactic scales (Harrison 2017; Storchi-Bergmann & Schnorr-Müller 2019; Riffel et al. 2022; Couto & Storchi-Bergmann 2023; Nandi et al. 2023a; Yang et al. 2024). Theoretical studies do invoke feedback to understand galaxy evolution (Ward et al. 2022 and references therein). Also, simulations do find quenching of SF in galaxies with AGN feedback (Byrne et al. 2023). A viable feedback mechanism is AGN outflows, which can impact the SF characteristic of AGN hosts by either suppressing (negative feedback process; Harrison 2017; Hervella Seoane et al. 2023; Nandi et al. 2023b) or enhancing (positive feedback process; Maiolino et al. 2017; Gallagher et al. 2019; Zhuang et al. 2021) SF. Also, both processes could coexist in a galaxy, as has been recently observed (Zinn et al. 2013; Shin et al. 2019; García-Bernete et al. 2021).

One possibility to study the impact of AGN on the SF characteristics of their hosts is to map the star-forming regions in galaxies hosting AGN and look for any correlations between the deduced SF and AGN properties. It is natural to expect that the influence of the central AGN on their hosts could decrease from the center to the outskirts of the galaxy (Tsai & Hwang 2015). While simulations (Bollati et al. 2023) and observations (Lammers et al. 2023) favor feedback processes to operate in the central kiloparsec region, their effect on the galaxy at the few tens of kiloparsecs scale is uncertain (Fiore et al. 2017). In the nearby Universe, Seyfert-type AGN are ideal targets to investigate this connection as the resolution offered by ground-based imaging observations will enable one to probe SF on scales from a few hundred parsecs to a few tens of kiloparsecs. Circumnuclear SF is generally observed in this category of AGN (Davies et al. 1998; Álvarez-Álvarez et al. 2015; Hennig et al. 2018; Diniz et al. 2019). They have also been studied for SF for more than three decades on different spatial scales as well as at different wavelengths (Gu et al. 2001; Cid Fernandes et al. 2004; Davies et al. 2007; Bing et al. 2019; Riffel et al. 2022; Zhang & Ho 2023). Despite years of research, the nature of SF in AGN host galaxies vis-à-vis normal galaxies is not settled and is highly debated. For example, in a nearby dwarf Seyfert-type AGN, NGC 4395, Nandi et al. (2023a) found regions of high SF close to the center, which could be due its AGN activity. Considering the far-infrared emission to be due to SF, Rodriguez Espinosa et al. (1987) found that the far-infrared luminosities of Seyfert galaxies and starburst galaxies are indistinguishable and argued for the bulk of the far-infrared emission in Seyfert galaxies to be due to SF. Alternatively, García-González et al. (2016) found that in a few of the Seyfert galaxies studied by them, the bulk of the nuclear far-infrared luminosity is contributed by the dust heated by the AGN. Cid Fernandes et al. (2004) studied SF history extensively in type 2 Seyfert galaxies and found that

Table 1
Details of the Sources Analyzed in This Work

Name	R.A. (J2000)	Decl. (J2000)	z	Scale (pc arcsec^{-1})	Morphology	AGN Type	M_* ($M_\odot$)	R_{25} (arcmin)	$A(V)$ (mag)
NGC 1365	03:33:36.37	−36:08:25.45	0.005	124.4	SB(s)b	Sy 1.8	10.71 ± 0.10 (a)	5′.61, 3′.08, 32°	0.056
NGC 4051	12:03:09.61	44:31:52.80	0.002	41.5	SAB(rs)bc	NLSy1	10.13 ± 0.25 (b)	2′.62, 1′.94, 135°	0.036
NGC 4151	12:10:32.58	39:24:20.63	0.003	62.3	(R′)SAB(rs)ab	Sy 1.5	10.40 ± 0.25 (b)	3′.15, 2′.13, 50°	0.074
NGC 4321	12:22:54.83	15:49:19.54	0.005	103.7	SAB(s)bc	LINER	10.83 ± 0.28 (c)	3′.71, 3′.15, 30°	0.072
NGC 4388	12:25:46.75	12:39:43.51	0.008	165.8	SA(s)b	Sy 1.9	10.42 (d)	2′.81, 0′.64, 92°	0.091
NGC 5033	13:13:27.47	36:35:38.17	0.003	62.3	SA(s)c	Sy 1.9	11.01 ± 0.2 (e)	5′.36, 2′.51, 170°	0.032
NGC 6814	19:42:40.64	−10:19:24.57	0.005	103.7	SAB(rs)bc	Sy 1.5	10.34 ± 0.29 (b)	1′.51, 1′.41	0.509
NGC 7469	23:03:15.62	08:52:26.39	0.016	331.0	(R′)SAB-(rs)a	Sy 1.2	10.88 ± 0.23 (b)	0′.74, 0′.54, 125°	0.188

Note. Here, R.A., decl., redshift (z), morphology, AGN type, and the extinction in the V band, $A(V)$, are from the NASA/IPAC Extragalactic Database (NED). Here, (a) is from Parkash et al. (2018), (b) is from Bentz & Manne-Nicholas (2018), (c) is from Georgiev et al. (2016), (d) is from Andreani et al. (2018), (e) is from Sweet et al. (2018), M_* is the stellar mass, and R_{25} is the radius of the galaxy to an optical surface brightness limit of 25 mag arcsec^{-2} taken from NED.

they are heterogeneous and host a mixture of young, intermediate, and old stellar populations.

To gain a comprehensive understanding of SF in galaxies, it is crucial to employ a range of wavelength bands. This is because galaxies contain diverse stellar populations and multiphase interstellar medium (ISM), making it necessary to utilize various tracers for SF across the electromagnetic spectrum, from X-ray to radio wavelengths. In this context, radio and millimeter-wave bands serve as tracers for SF activity via their continuum and molecular line emission. On the other hand, Hα and ultraviolet (UV) emissions act as indicators of ionizing radiation emitted by hot stars. Sometimes, the continuum UV photons interact with the surrounding gas and dust in the ISM, giving rise to infrared (IR) emissions. Hα emission is particularly informative as it reveals the presence of stellar populations with ages ranging from 1 to 10 million years. UV emission, on the other hand, primarily traces young, massive star clusters, providing insights into stellar populations aged between 10 and 100 million years (Kennicutt & Evans 2012). It is worth emphasizing that the presence of dust within a galaxy can diminish the intensity of UV light emitted by stars by either scattering or absorbing UV photons. Nevertheless, accounting for this extinction effect and applying suitable corrections can yield accurate and valuable results.

Until now, most studies of SF in Seyfert galaxies have been conducted in the optical, IR, or radio wavelengths using ground-based and space-based observatories. While there have been a few studies in the UV band using the Galaxy Evolution Explorer (GALEX; Martin et al. 2005), the resolution provided by GALEX is often insufficient to resolve SF on parsec scales. A limited number of studies have used the Hubble Space Telescope, which offers the capability to resolve parsec-scale structures, but it has a restricted field of view (FOV), making it observationally expensive to study a large number of sources comprehensively. To address this gap, we have undertaken a systematic investigation of the SF properties of Seyfert galaxies using the Ultraviolet Imaging Telescope (UVIT). This telescope provides moderate angular resolution, better than 1″.5 (Tandon et al. 2020), and offers good FOV coverage, approximately ∼28′ diameter. In Section 2, we describe our source selection process. Section 3 outlines our observations and data reduction procedures. In Section 4, we describe the methods we used for our analysis. In Section 5, we present our research findings on each of the objects studied in this work. The global picture of the results of this work is given in Section 6, followed by the summary in the final section. In this work, we considered a flat ΛCDM cosmology with $H_0 = 70 \, \text{km s}^{-1} \, \text{Mpc}^{-1}$, $\Omega_\Lambda = 0.7$, and $\Omega_m = 0.3$.

2. Our Sample

Our sample of sources for this study was selected primarily from the catalog of Véron-Cetty & Véron (2006). Our initial criteria involved the identification of objects classified as Seyferts in the Véron-Cetty & Véron (2006) catalog with redshift $z < 0.02$. This redshift cut was imposed so that at the resolution of the UVIT (Tandon et al. 2020), the minimum spatial scale that could be probed is about few tens of parsecs. We manually inspected our sample of Seyfert-type AGN in the GALEX database to assess their UV emission. Additionally, we imposed a size constraint, requiring that the selected objects have an angular size exceeding 2′ but less than 12′. We also considered some nearby low-ionization nuclear emission-line region (LINER) types of AGN for which UVIT observations are already available and satisfy the above criteria. This resulted in the identification of 30 objects. We have acquired observations for few sources in our sample. We aim to complete observations of the remaining targets with UVIT in the upcoming observing cycles. Results on one source in our sample, namely NGC 4395, are reported in Nandi et al. (2023a), while in this paper we report the results on another eight sources. The details of the sources are given in Table 1.

3. Observations and Data Reduction

The observations of our sample of sources were made using UVIT (Tandon et al. 2020), one of the payloads on board AstroSat (Agrawal 2006), India's multiwavelength astronomical observatory launched by the Indian Space Research Organization on 2015 September 28. UVIT observes simultaneously in the far-ultraviolet (FUV; 1300−1800 Å) and the near-ultraviolet (NUV; 2000−3000 Å) over a ∼28′ diameter field with a spatial resolution better than 1″.5 in multiple filters. The FUV and NUV channels operate in the photon counting mode, while the VIS channel (VIS; 3200−5500 Å) operates in the integration mode. Images from the VIS channel are used for monitoring the drift of the satellite. For the sources in this study, we used the data available in the archives of the Indian Space Science Data Center (ISSDC[5]). From ISSDC, we directly took the science-ready images for further analysis in

---

Table 2
Summary of Observations

Name	Observation ID (OBSID)	PI	Date	Filter		Exposure Time (s)	
				FUV	NUV	FUV	NUV
NGC 1365	A02_006T01_9000000776	Gulab	08/11/2016	F169M	N279N	24,905	37,833
	A02_006T01_9000000802	Gulab	17/11/2016				
	A02_006T01_9000000934	Gulab	28/12/2016				
NGC 4051	G05_248T01_9000000486	Stalin	11/02/2018	F172M	N219M	26,444	35,336
	G08_071T01_9000001888	KPSingh	11/02/2018				
NGC 4151	G06_117T01_9000001012	KPSingh	08/02/2017	F154W	N219M	67,547	73,548
	G06_117T01_9000001046	KPSingh	22/02/2017				
	G06_117T01_9000001086	KPSingh	17/03/2017				
	G08_064T01_9000001814	KPSingh	04/01/2018				
	G08_064T01_9000002070	KPSingh	02/05/2018				
NGC 4321	A08_003T05_9000003426	Hutchings	11/01/2020	F154W	⋯	6296	⋯
NGC 4388	A02_024T01_9000001044	Labani	21/02/2017	F154W	N245M	13,520	13,621
NGC 5033	G06_087T04_9000001028	Stalin	14/02/2017	F148W	N279N	2930	2948
NGC 6814	A05_037T01_9000003140	Pranoti	02/09/2019	F154W	⋯	46,782	⋯
NGC 7469	G08_071T02_9000001620	KPSingh	18/10/2017	F172M	N245M	34,493	50,032

Table 3
Details of the Filters Used in This Work (Tandon et al. 2020)

Filter Name	λ_{mean} (Å)	$\Delta\lambda$ (Å)
F148W	1481	500
F154W	1541	380
F169M	1608	290
F172M	1717	125
N219M	2196	270
N245M	2447	280
N279N	2792	90

Note. Here, λ_{mean} and $\Delta\lambda$ are the mean wavelength and the bandwidth in angstroms.

this work. These science-ready images were generated by the UVIT Payload Operations Center using the UVIT-L2 pipeline (Ghosh et al. 2022) and transferred to ISSDC for archiving and dissemination. The observational details of the sources used in this study are given in Table 2. Of the eight sources, six have observations at both the FUV and NUV wavelengths, while two have observations only at FUV wavelengths. The details of the filters used are given in Table 3.

For some sources, the filter-wise combined images taken from ISSDC have exposure times shorter than the sum of those of the individual orbit-wise images. Also, the final astrometry has large errors. Therefore, we used the orbit-wise L2 data, and aligned them and combined them filter-wise using the IRAF software package. To ensure precise astrometry of the combined images, we used the Gaia-EDR3 catalog (Gaia Collaboration et al. 2023), and carried out astrometry as elaborated in Nandi et al. (2023a). The measured count rates of the sources of interest were converted to physical units using the calibrations given in Tandon et al. (2020). For objects observed multiple times, to generate the final combined images, we used only those orbit-wise images having sufficient signal. The red–green–blue (RGB) images of the eight sources obtained using the final FUV and NUV images from UVIT along with archival optical images are shown in Figure 1.

4. Analysis

The motivation for this work is to understand the SF characteristics of the host galaxies of AGN. This involves detection of star-forming regions in the galaxies. For this we used the SExtractor module (Bertin & Arnouts 1996) in Python. To identify star-forming regions within each galaxy we adopted a 5σ threshold criterion and followed the details outlined in Nandi et al. (2023a). These identified star-forming regions might have contamination from foreground objects. To remove such foreground objects, we crossmatched the identified regions with the Gaia-DR3 (Gaia Collaboration et al. 2023) catalog, setting a cutoff in the proper motion of the regions at $10\,\mathrm{mas\,yr^{-1}}$. If a detected SF region had a counterpart within $2''$ in the Gaia catalog with a proper motion exceeding $10\,\mathrm{mas\,yr^{-1}}$, we excluded that SF region from our analysis. Thus, in total we identified 418 regions in NGC 1365, 131 regions in NGC 4051, 161 regions in NGC 4151, 340 regions in NGC 4321, 20 regions in NGC 4388, 557 regions in NGC 5033, 89 regions in NGC 6814, and 26 regions in NGC 7469. These identified regions for all the galaxies are marked and are shown in Figure 2.

The sizes of the identified star-forming regions varied, ranging from the point-spread function (PSF) of the instrument to approximately $4-5$ times its size. To correct for the instrumental resolution, we adopted an assumption of elliptical light distribution within the aperture, following the approach given in Nandi et al. (2023a). These corrected apertures were subsequently utilized for further analysis. The distribution of the areas of the identified star-forming regions in each of the galaxies is shown in Figure 3. We determined the flux of each of the star-forming regions via aperture photometry, using photutils package (Bradley et al. 2020). We corrected these flux measurements for extinction. To correct for Milky Way extinction, we relied on the prescription from Cardelli et al. (1989), and to correct for internal extinction, we used the UV slope (β) method (Calzetti et al. 2000). For measurements in two UV filters, one in FUV and the other in NUV, β was
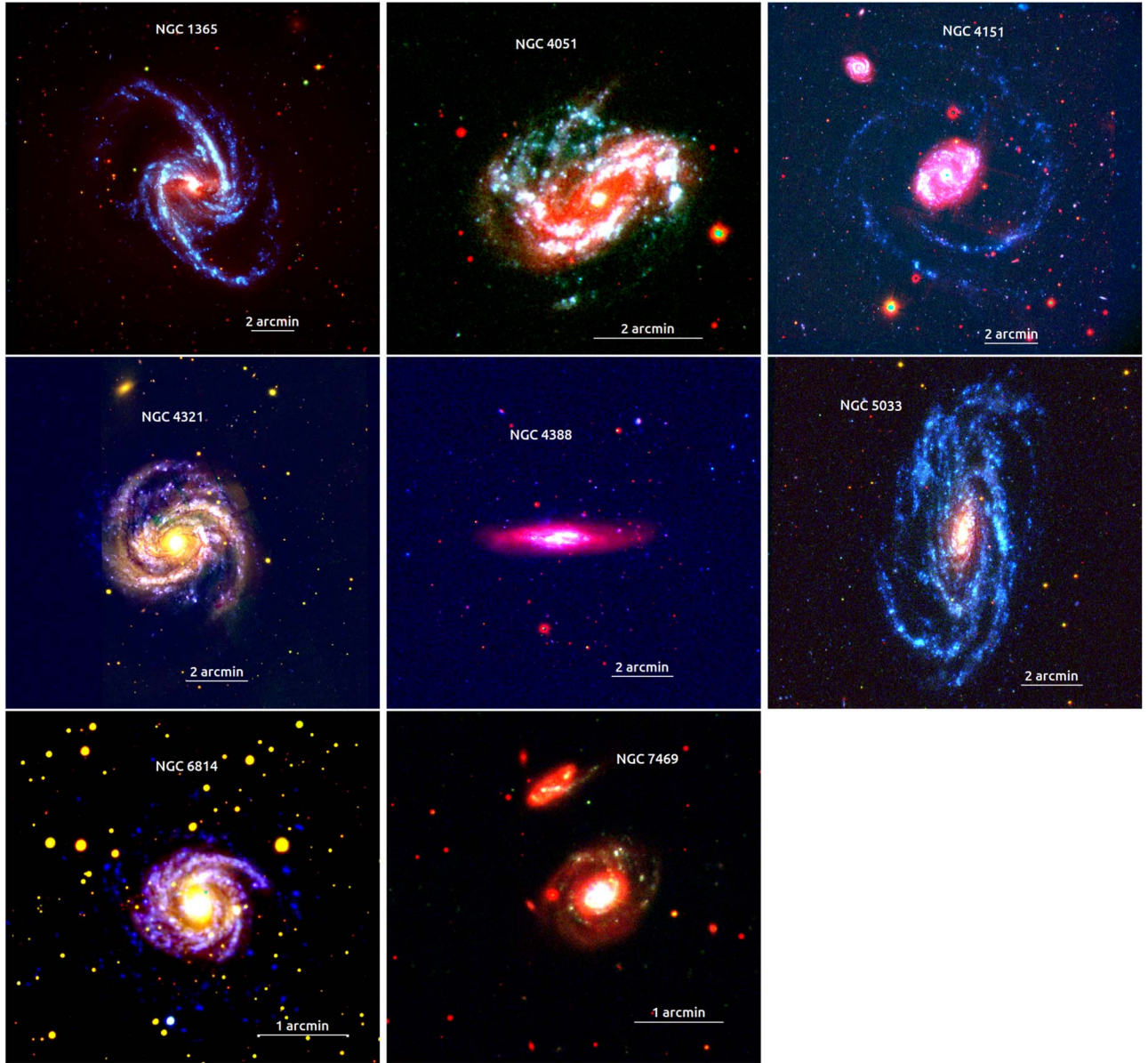
Figure 1. RGB images of the sources. Here, red is Pan-STARRS r band (except for NGC 1365, where it is from the Decadal Legacy Survey), green is UVIT NUV (except for NGC 4321 and NGC 6814, where it is Pan-STARRS g band), and blue is UVIT FUV.

calculated as

$$\beta = \frac{m_{\rm FUV} - m_{\rm NUV}}{-2.5\log(\lambda_{\rm FUV}/\lambda_{\rm NUV})} - 2.0. \quad (1)$$

Here, $m_{\rm FUV}$ and $m_{\rm NUV}$ are the magnitudes in FUV and NUV filters with wavelengths $\lambda_{\rm FUV}$ and $\lambda_{\rm NUV}$ respectively. The values of β give an idea of the dust obscuration in the star-forming regions. Using the calculated β, we estimated the color excess, $E(B-V)$, using the following relation:

$$E(B - V) = (\beta + 2.616)/4.684. \quad (2)$$

The distributions of the $E(B-V)$ values for the identified star-forming regions are given in Figure 4. We estimated the internal extinction at any particular wavelength λ as

$$A_\lambda = 0.44 \times E(B - V) \times k'(\lambda), \quad (3)$$

where $k'(\lambda)$ is from Calzetti et al. (2000).

In cases where NUV data from UVIT were unavailable, we calculated the UV slope using two FUV filters. For regions where neither FUV and NUV filters nor two FUV filters were available from UVIT, we utilized the GALEX FUV and NUV images. In such instances, we convolved the instrument-corrected aperture with the GALEX PSF and employed those apertures to determine the extinction correction. The spatial and radial variations of internal extinction for our sample of galaxies are shown in Figure 5.

After getting the extinction value for each SF region, we calculated the intrinsic luminosities of the star-forming regions and used them to estimate the star formation rate (SFR) at NUV and FUV wavelengths as follows (Salim et al. 2007):

$$\log[{\rm SFR}_{\rm FUV}(M_\odot\,{\rm yr}^{-1})] = \log[L_{\rm FUV}({\rm W\,Hz}^{-1})] - 21.16 \quad (4a)$$

$$\log[{\rm SFR}_{\rm NUV}(M_\odot\,{\rm yr}^{-1})] = \log[L_{\rm NUV}({\rm W\,Hz}^{-1})] - 21.14. \quad (4b)$$
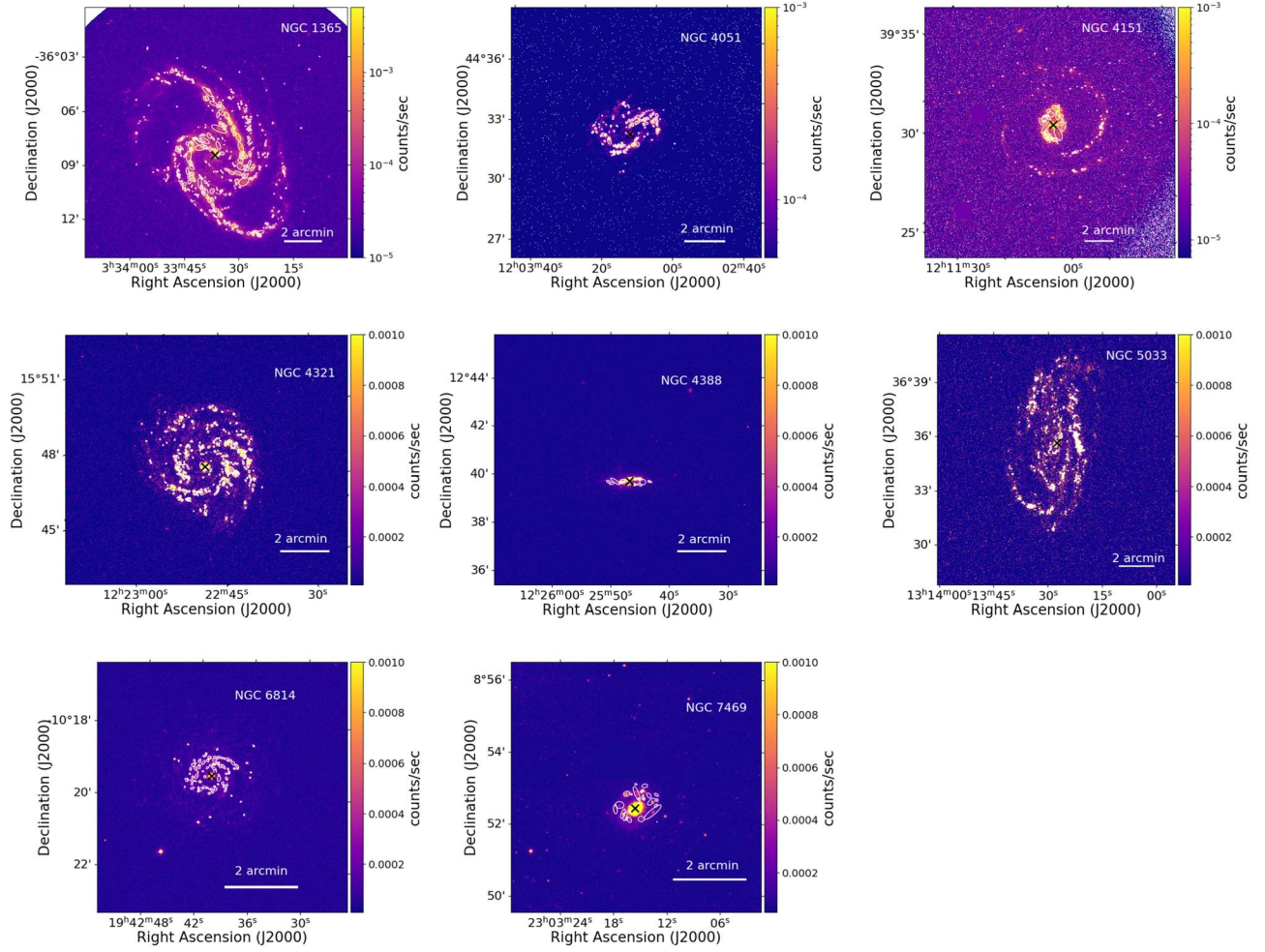
Figure 2. FUV images of the objects with the identified star-forming regions marked by white ellipses. The central AGN is marked by a black cross.

We calculated the surface density of SFR (Σ_{SFR}) by taking the ratio of the SFR to the area of the star-forming regions. The spatial and radial variations of Σ_{SFR} values for our sample of sources are shown in Figure 6. A summary of the star-forming regions in each galaxy is provided in Table 4.

5. Notes on Individual Sources

5.1. NGC 1365

NGC 1365 at a redshift $z = 0.005$ (de Vaucouleurs et al. 1991) is a face-on barred spiral galaxy of SB(s)b type (de Vaucouleurs et al. 1991) and harbors a type 1.8 Seyfert AGN (Maiolino & Rieke 1995) with a black hole of mass $M_{\text{BH}} \sim 10^{6.5} M_{\odot}$ (Risaliti et al. 2009). NGC 1365, with an X-ray luminosity of $L_{2-10\text{keV}} = 10^{42}$ erg s^{-1} (Risaliti et al. 2005), is variable in X-rays, exhibiting variability on timescales of hours to years (Brenneman et al. 2013). Notably, NGC 1365 is host to a rich population of star clusters and is a prominent galaxy within a 30 Mpc distance (Whitmore et al. 2023). At radio frequencies, detection of a ringlike structure in the circumnuclear region with multiple knots of emission was reported by Saikia et al. (1994). This was followed by a more detailed study, which showed the knots of emission to have a nonthermal spectrum, and a suggestion of a possible jetlike structure at a position angle (PA) $\sim 125°$ (Sandqvist et al. 1995). Stevens et al. (1999) confirm the nonthermal nature of

the knots and suggest that these are mostly due to multiple supernova remnants. They also suggest that the jetlike structure could be due to a nuclear bar that extends to the ring.

We identified 418 star-forming regions, with the faintest region of 23.56 mag in FUV, while the brightest region has a brightness of 13.70 mag in the same FUV band. In the NUV, the faintest and the brightest SF regions have brightnesses of 23.81 mag and 12.79 mag respectively. These star-forming regions span a broad range of sizes, ranging from 0.042 to 11.93 kpc^2, with average and median values of 0.713 and 0.215 kpc^2 respectively.

We found the color excess, $E(B - V)$, to vary from 0.019 to 0.783 mag, with an average of 0.212 mag and a median of 0.195 mag. In the FUV band, the extinction ranged from 0.08 to 3.428 mag, with an average of 0.93 mag and a median of 0.86 mag. Meanwhile, in the NUV band, the extinction values range from 0.06 to 2.51 mag, with a median of 0.63 mag and an average of 0.68 mag. We found higher extinction in the inner regions than in the outer regions (see Figure 5). Σ_{SFR} for the star-forming regions in NGC 1365 varied between 1.268×10^{-3} and $22.96 \times 10^{-2} M_{\odot}$ yr^{-1} kpc^{-2} in the FUV band, with an average Σ_{SFR} of $8.91 \times 10^{-3} M_{\odot}$ yr^{-1} kpc^{-2}. Similarly, in the NUV band, we found the Σ_{SFR} values to vary between 9.72×10^{-4} and $55.62 \times 10^{-2} M_{\odot}$ yr^{-1} kpc^{-2}, with a average of $11.19 \times 10^{-3} M_{\odot}$ yr^{-1} kpc^{-2}. We found the distribution of the Σ_{SFR} values in both FUV and NUV to be
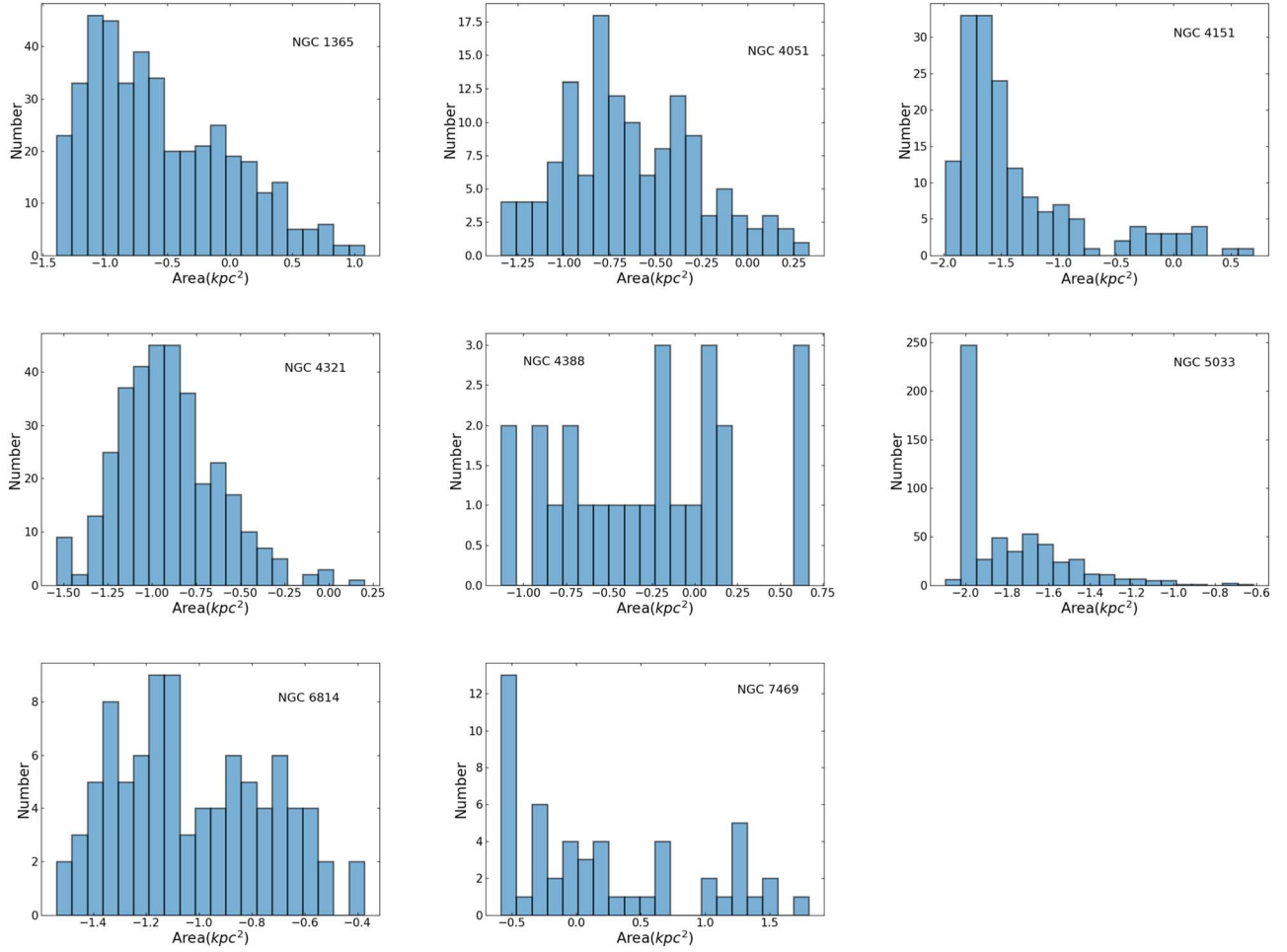
Figure 3. Distributions of the areas (log scale) of the identified star-forming regions in the sources studied in this work. The names of the sources are given in their respective panels.

similar. We found the extinction and Σ_{SFR} to decrease radially outwards, as can be seen in Figures 5 and 6 respectively. The details of the SF regions are given in Table 6.

5.2. NGC 4051

NGC 4051, an intermediate barred spiral galaxy with a morphological type of SAB(rs)bc (de Vaucouleurs et al. 1991; Evans et al. 1996), is at a redshift of $z = 0.002$ (Véron-Cetty & Véron 2006). It is a narrow-line type 1 Seyfert galaxy (Khachikian & Weedman 1974) and powered by a black hole of mass $6 \times 10^5 M_\odot$ (Seifina et al. 2018). It is luminous in X-rays with $L_{2-10\mathrm{keV}} = 2.7 \times 10^{41}$ erg s^{-1} (Pounds et al. 2004), and is known to be variable across wavelengths and timescales (Peterson et al. 2000; McHardy et al. 2004; Jones et al. 2011; Kumari et al. 2023). High-resolution observations at radio frequencies such as with the Very Large Array (VLA) A-array at 8.4 GHz show a core and two distinct components on opposite sides, while lower-resolution observations do not resolve this inner triple well but exhibit more diffuse extended emission (e.g., Jones et al. 2011). Unlike at X-ray wavelengths, they do not find evidence of significant variability of the core at radio frequencies. From continuum-subtracted Hα images, Evans et al. (1996) identified numerous H II knots within its spiral arms.

We detected 131 star-forming regions having FUV brightness between 23.97 mag (the faintest) and 16.55 mag (the brightest). Similarly, in the NUV band, the star-forming regions varied in brightness between 24.40 mag at the faintest end and 16.69 mag at the brightest end. The areas of these star-forming regions have a wide range, varying from 0.046 kpc^2 to 2.144 kpc^2, with average and median values of 0.341 kpc^2 and 0.207 kpc^2 respectively.

We found the $E(B-V)$ values to span a wide range from -0.357 to 0.418 mag, with an average of value of -0.046 mag and a median value of -0.038 mag. Extinction in the FUV band is found to vary between -1.51 and 1.77 mag, while we found the extinction values in the NUV band to vary between -1.32 and 1.55 mag, with mean and median values of -0.17 mag and -0.14 mag, respectively.

We found Σ_{SFR} of the star-forming regions to have a wide range between 1.09×10^{-4} and $42.79 \times 10^{-4} M_\odot$ yr^{-1} kpc^{-2} in the case of FUV and between 8.1×10^{-5} and $41.22 \times 10^{-4} M_\odot$ yr^{-1} kpc^{-2} in the case of NUV. The average Σ_{SFR} in the FUV and NUV bands are $7.72 \times 10^{-4} M_\odot$ yr^{-1} kpc^{-2} and $6.98 \times 10^{-4} M_\odot$ yr^{-1} kpc^{-2} respectively. We found the Σ_{SFR} values to be similar in both FUV and NUV bands.

5.3. NGC 4151

NGC 4151, with a well-defined spiral pattern and a central bulge (de Vaucouleurs et al. 1991; Mundell et al. 1999), is an intermediate face-on spiral galaxy with a morphology of (R') SAB(rs)ab. It hosts a type 1.5 Seyfert AGN (Véron-Cetty &
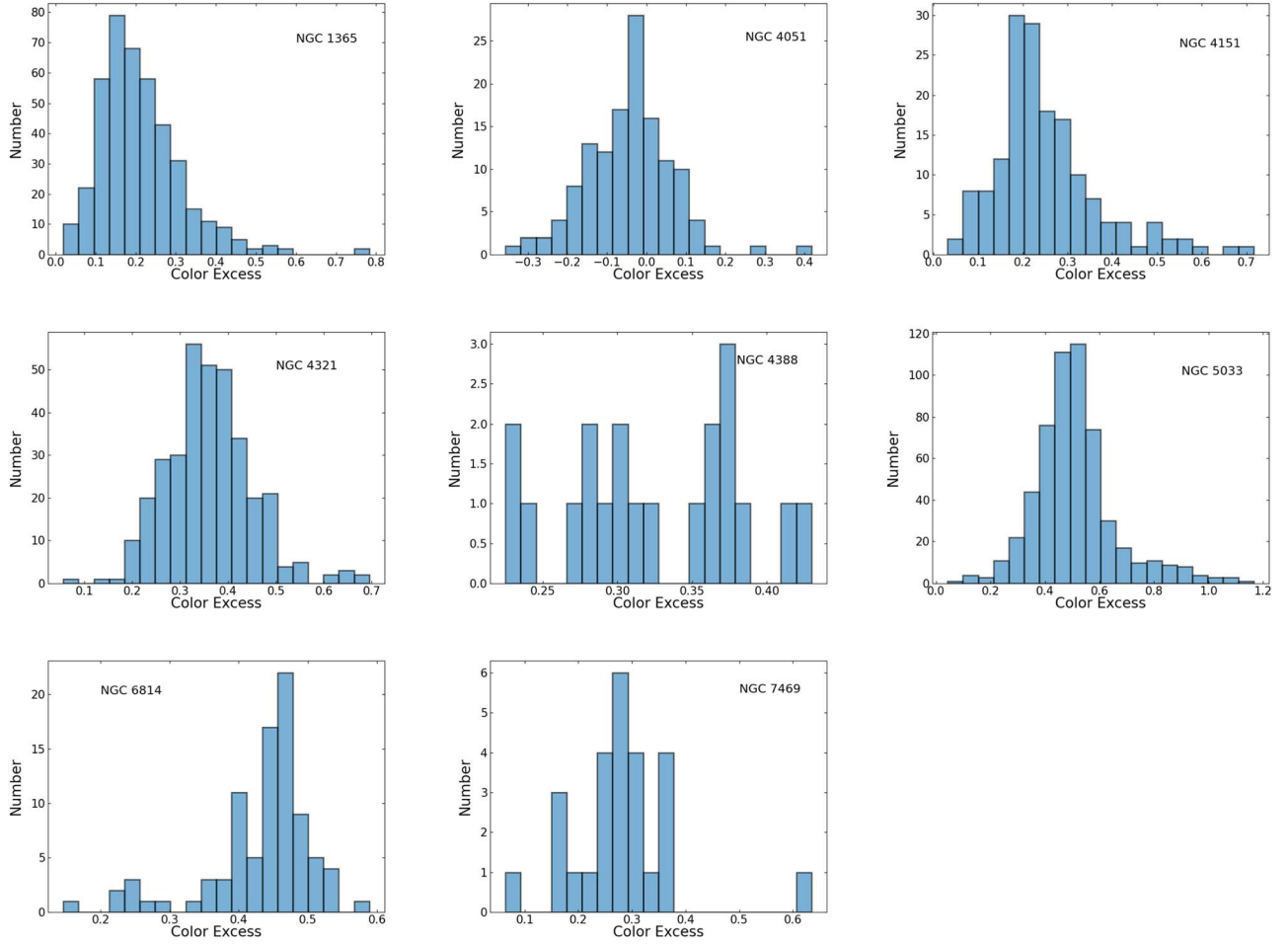
Figure 4. Distributions of $E(B - V)$ of the identified star-forming regions in the sources studied in this work. The names of the sources are given in their respective panels.

Véron 2006), is situated at a redshift of $z = 0.0033$ (Wolfinger et al. 2013), and is powered by a black hole of mass $4.57 \times 10^7 M_\odot$ (Bentz et al. 2006). Its X-ray luminosity ranges between (1.3 and 2.1) $\times 10^{42}$ erg s^{-1} (Wang et al. 2010) and has been studied for variability over a wide range of wavelengths. It has a two-sided radio jet, and the gas-rich spiral arms, along with the bar, are prominently visible in H I images (Bosma et al. 1977). The outer spiral arms are clearly visible in both FUV and NUV images, as can be seen in Figures 1 and 2. These two distinct spiral arms are not prominent in the optical band but are nicely traced by H I observation (Pedlar et al. 1992). The radio structure of NGC 4151 has been studied for decades. It exhibits a two-sided jet with multiple components at a PA $\sim 77°$, with one of the components (C4) coincident with the optical nucleus of the galaxy. C4, which is presumably associated with the super-massive black hole at its center, was found to vary at radio frequencies, but no significant motion was detected between C4 and the nearby C3 component over a 22 yr period (Williams et al. 2017).

We detected 161 star-forming regions. The faintest and the brightest star-forming regions identified by us in the FUV image of NGC 4151 have magnitudes of 23.76 mag and 16.36 mag, respectively. Similarly, in the NUV band, the faintest and the brightest star-forming regions detected have brightness values of 23.91 mag and 16.25 mag respectively. These star-forming regions have a wide range of areas between

0.010 kpc^2 and 4.921 kpc^2, with average and median areas of 0.188 kpc^2 and 0.027 kpc^2 respectively. We found the color excess, $E(B - V)$, to vary between 0.032 and 2.446 mag, with an average value of 0.252 mag and a median value of 0.227 mag. Extinction in the FUV band varied between 0.15 and 3.21 mag, with an average of 1.13 mag and a median of 1.02 mag, while in the NUV band, extinction varied from 0.12 to 2.66 mag, with a median of 0.94 mag and a average of 0.843 mag.

The estimated Σ_{SFR} of these SF regions exhibited a wide range, with Σ_{SFR} values in the FUV band varying from 8.55×10^{-4} to $0.05 M_\odot$ yr^{-1} kpc^{-2}. The average Σ_{SFR} in the FUV band is $48.40 \times 10^{-4} M_\odot$ yr^{-1} kpc^{-2}. In the NUV band, Σ_{SFR} values ranged between 7.72×10^{-4} and $0.07 M_\odot$ yr^{-1} kpc^{-2} with an average Σ_{SFR} of $57.11 \times 10^{-4} M_\odot$ yr^{-1} kpc^{-2}. The detailed properties of the star-forming regions are given in Table 6.

5.4. NGC 4321

NGC 4321, classified as a late-type, nearly face-on grand design spiral galaxy with an SAB(s)bc morphology (de Vaucouleurs et al. 1991), is at a redshift of $z = 0.00524$ (Allison et al. 2014) and is powered by a black hole of mass $(2.5 \pm 0.2) \times 10^7 M_\odot$ (Sarzi et al. 2002). It has two bars and a circumnuclear ring (Garcia-Burillo et al. 1998). It is categor-ized as H II/LINER and exhibits a relatively high X-ray luminosity, exceeding 1.9×10^{40} erg s^{-1} (González-Martín
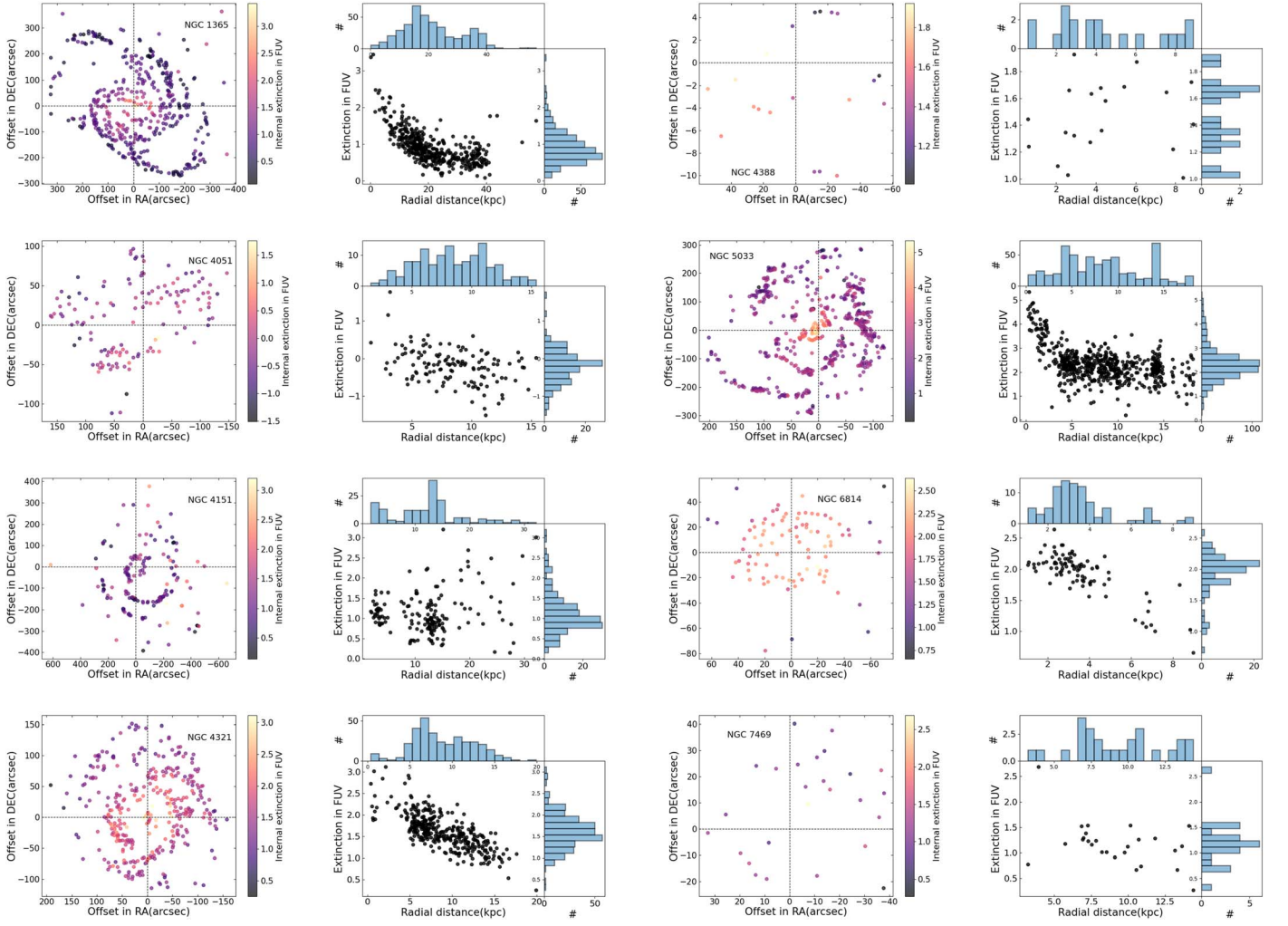
Figure 5. Spatial (left panel) and radial (right panel) variations of internal extinction for each source.

et al. 2009). In the radio, the image made with the Effelsberg telescope with an angular resolution of $\sim71''$ shows a bright central region and an extended disk (Urbanik et al. 1986). Higher-resolution observations with the VLA with an angular resolution of $2''$ showed the central region to have a roughly circular structure with an angular extent of $\sim20''$. Radio emission appears to peak at the optical nucleus and also at an enhanced region $\sim7''$ to the east near an optical condensation, besides emission from SN 1979c (Weiler et al. 1981). Moreover, strong activity has been observed across optical and radio wavelengths, leading to the classification of NGC 4321 as a transition galaxy, bridging the gap between normal and AGN galaxies (Immler et al. 1998).

NGC 4321 has giant molecular associations in various regions, including the bar, spiral arms, and circumnuclear ring (Pan & Kuno 2017). It has been observed that SF is most active within the circumnuclear ring, with lower activity occurring in the interarm regions (Pan & Kuno 2017). SF in the circumnuclear region or nuclear rings is attributed to bursts triggered by the inner Lindblad resonance (Arsenault 1989). Additionally, Hα emission is prominent on the leading side of the bar and spiral arms, contributing to the understanding of star-forming regions in the galaxy (Pan & Kuno 2017). Further studies, such as those by Ferreras et al. (2012), have investigated young star-forming regions in the NUV and

optical ranges. While these studies confirmed the association of Hα emission with the nuclear region, they did not find a significant correlation between the distance from these regions and the age or dust content.

We identified 340 star-forming regions in NGC 4321. These regions have a wide range in brightness with values ranging between 22.19 and 13.92 mag in the FUV band. They have a range of sizes from 0.029 to 1.587 kpc^2, with an average area of 0.159 kpc^2 and a median of 0.116 kpc^2. The $E(B-V)$ values within these regions range between 0.056 and 0.695 mag, with average and median values of 0.361 mag and 0.356 mag respectively. We found the extinction in the FUV band to cover a wide range from 0.25 to 3.11 mag, with average and median of 1.62 mag and 1.59 mag, respectively.

Σ_{SFR} within these SF regions in the FUV band has a wide range from 5.82×10^{-3} to $55.17 \times 10^{-2} M_\odot \, \mathrm{yr}^{-1} \, \mathrm{kpc}^{-2}$, with an average Σ_{SFR} of $3.43 \times 10^{-2} M_\odot \, \mathrm{yr}^{-1} \, \mathrm{kpc}^{-2}$. Both extinction and Σ_{SFR} were found to show a gradual decline from the center toward the outer regions of the galaxy as can be seen in Figures 5 and 6.

5.5. NGC 4388

NGC 4388 is a nearly edge-on spiral galaxy, classified as type SA(s)b with a major-axis PA of $91°$ (de Vaucouleurs et al. 1991;
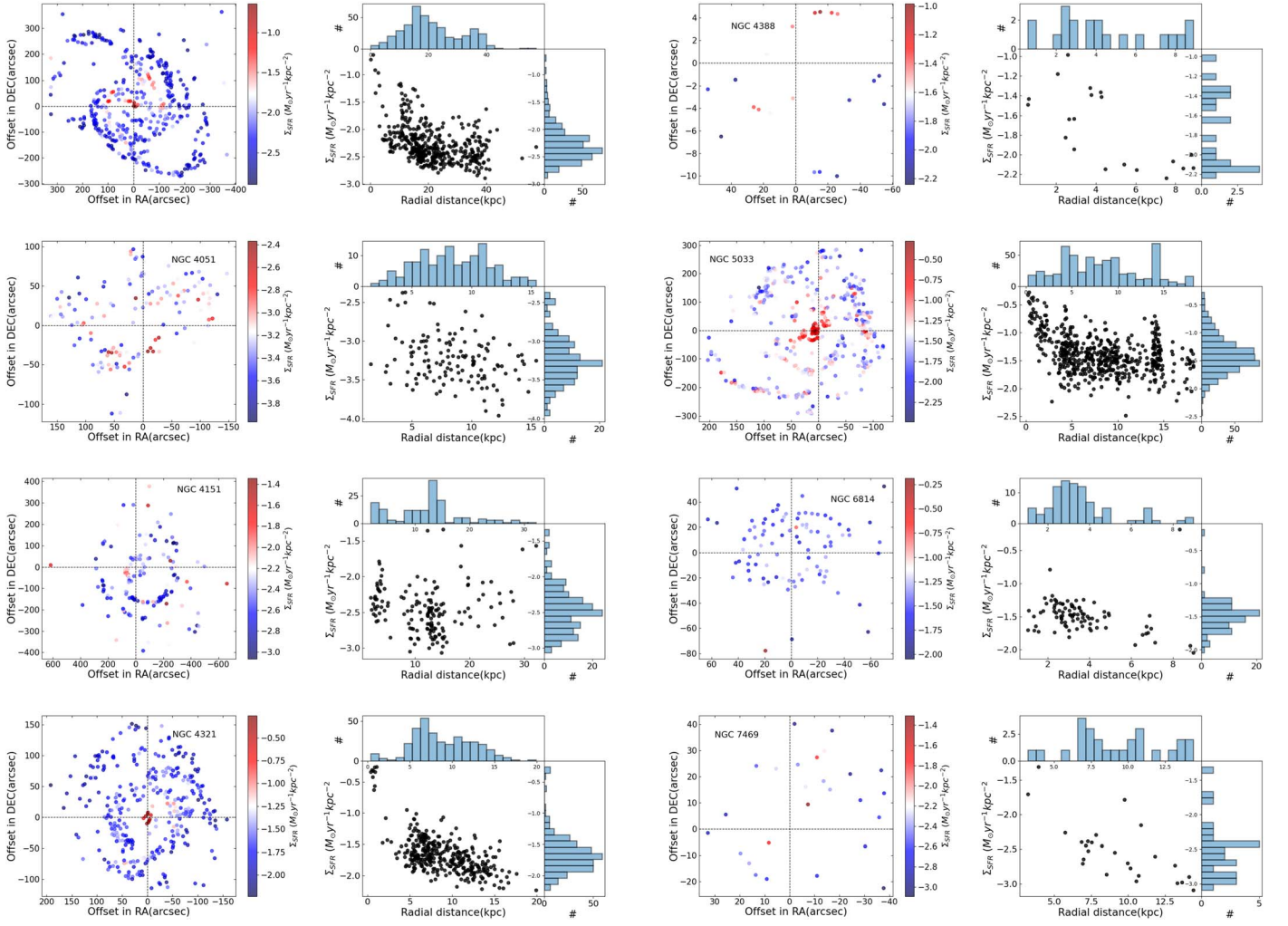
Figure 6. Spatial (left panel) and radial (right panel) variations of Σ_{SFR} on a log scale.

Table 4
Summary of the Identified Star-forming Regions for All Sources

Name	N	Mean						Median					
		Area (kpc^2)	$E(B-V)$ (mag)	A_{FUV} (mag)	A_{NUV} (mag)	Σ_{SFR}^{FUV}	Σ_{SFR}^{NUV}	Area (kpc^2)	$E(B-V)$ (mag)	A_{FUV} (mag)	A_{NUV} (mag)	Σ_{SFR}^{FUV}	Σ_{SFR}^{NUV}
NGC 1365	418	0.713	0.212	0.93	0.68	8.90	11.19	0.215	0.195	0.86	0.63	4.65	4.83
NGC 4051	131	0.341	−0.046	−0.19	−0.17	0.77	0.70	0.207	−0.038	−0.16	−0.14	0.54	0.48
NGC 4151	161	0.187	0.252	1.13	0.94	4.84	5.71	0.027	0.227	1.02	0.84	3.32	3.56
NGC 4321	340	0.159	0.356	1.62	⋯	34.37	⋯	0.116	0.36	1.60	⋯	20.02	⋯
NGC 4388	20	1.268	0.325	1.46	1.13	27.23	31.38	0.755	0.318	1.43	1.11	19.04	23.05
NGC 5033	557	0.021	0.509	2.33	1.63	57.73	128.34	0.013	0.494	2.26	1.58	37.75	62.33
NGC 6814	89	0.120	0.432	1.94	⋯	41.96	⋯	0.083	0.452	2.03	⋯	32.95	⋯
NGC 7469	26	12.026	0.277	1.17	0.96	5.71	7.08	4.973	0.277	1.17	0.97	2.66	2.88

Note. The values of Σ_{SFR} are in units of $10^{-3}\ M_\odot\ \mathrm{yr}^{-1}\ \mathrm{kpc}^{-2}$.

Paturel et al. 2003). Located at a distance of approximately 37.55 Mpc corresponding to a redshift of $z = 0.00842$ (Lu et al. 1993), this galaxy exhibits a short bar whose strength depends on the eccentricity of stellar or gas orbits (Veilleux et al. 1999). At its center, NGC 4388 hosts a type 2 Seyfert AGN with a supermassive black hole of mass $(8.4 \pm 0.2) \times 10^6\ M_\odot$ (Tueller et al. 2008; Kuo et al. 2011). It is a strong X-ray source, with an

X-ray luminosity of $L_{2-10\mathrm{keV}} = 1 \times 10^{42}\ \mathrm{erg\ s}^{-1}$ (Forster et al. 1999). VLA observations have revealed an elongated blob with an extent of $\sim 13''$ to the north of the galaxy and a collimated structure of $\sim 2.8''$ toward the south, the observed asymmetry possibly being due to an asymmetric distribution of ISM (Hummel & Saikia 1991). More recently, Sargent et al. (2024) have made a detailed study with the VLA in both total intensity

and linear polarization and have suggested that the radio continuum emission is due to AGN winds interacting with the local ISM.

NGC 4388 also exhibits significant dust obscuration, with dust bands extending to approximately 1.5 kpc from the center of the disk (Falcke et al. 1998). Studies have shown that the galaxy possesses a truncated H I disk and gas components outside the plane, suggesting a possible interaction with the intergalactic medium (Singh et al. 2019). This interaction is believed to have involved ram pressure stripping, resulting in the loss of approximately 85% of the H I gas component in NGC 4388, subsequently disrupting SF in the galaxy (Cayatte et al. 1990). Recent investigations have indicated star-forming regions not coplanar with the disk, contributing to the extended outflows and suggesting recent starburst events in the spiral arms and circumnuclear region of the galaxy (Damas-Segovia et al. 2016).

We detected 20 star-forming regions in NGC 4388. These regions have FUV brightness between 22.06 and 15.79 mag, while in the NUV the brightness of the star-forming regions varied between 22.07 and 15.72 mag. The areas of these regions were found to show considerable variation, spanning from 0.074 to 4.636 kpc^2, with an average area of 1.268 kpc^2 and a median of 0.754 kpc^2. The $E(B - V)$ values span a range from 0.23 to 0.43 mag, with an average of 0.33 mag and a median of 0.32 mag. Extinction values in the FUV band were found to have a wide range from 1.01 to 1.92 mag, with mean and median of 1.46 mag and 1.43 mag, respectively, while in the NUV band, extinction varied between 0.78 and 1.49 mag, with a median of 1.11 mag and an average of 1.13 mag. Σ_{SFR} within these regions in the FUV was found to vary between 5.74×10^{-3} and $103.79 \times 10^{-3} M_\odot \, yr^{-1} \, kpc^{-2}$. with an average Σ_{SFR} of $27.23 \times 10^{-3} M_\odot \, yr^{-1} \, kpc^{-2}$. Similarly, in the NUV band, we found Σ_{SFR} to range between 7.16×10^{-3} and $108.92 \times 10^{-3} M_\odot \, yr^{-1} \, kpc^{-2}$. We found an average Σ_{SFR} in the NUV band of $31.38 \times 10^{-3} M_\odot \, yr^{-1} \, kpc^{-2}$. Properties of the 20 individual star-forming regions are given in Table 6.

5.6. NGC 5033

NGC 5033 is an SA(s)c-type nonbarred spiral galaxy at a redshift of $z = 0.00291$. It has a central bulge with a mass of approximately $2 \times 10^{10} M_\odot$. It is a type 1.9 Seyfert galaxy, and hosts a supermassive black hole at its center, with a mass in the range $(5-12) \times 10^6 M_\odot$. It is luminous in X-rays with $L_{2-10keV} = 2.3 \times 10^{41} \, erg \, s^{-1}$ (Terashima et al. 1999). Although high-resolution radio observations show a core–jet morphology, the radio emission from the inner disk is dominated by a starburst with the core–jet structure contributing only 7% of the flux density at 1.4 GHz (Pérez-Torres & Alberdi 2007). They also report evidence of a "radio spur" due to a hot bubble caused by sequential supernova explosions. The galaxy is variable in X-ray wavelengths (Papadakis et al. 2008).

The galaxy's flat disk has a high inclination of $67°.5$ and shows signs of possible warping, possibly resulting from interactions or mergers. Near-infrared and millimeter observations reveal a small nuclear bar, while the presence of H II regions following a ringlike pattern is evident in Hβ intensity maps. A bright bar of light from the unresolved nucleus has been observed in NUV images. Radio studies of the 21 cm line show similarities between the H I distribution and optical characteristics, and it has been found that Σ_{SFR} is directly related to the total gas surface density. Comprehensive CO(1

−0) observations suggest that there is no starburst phenomenon in the nuclear region. Instead, star-forming regions are present in the disk region, which is supported by observations from the GALEX telescope. The radio and FIR luminosities of the inner regions indicate evidence of a recent short starburst in NGC 5033 (Pérez-Torres & Alberdi 2007).

We identified 557 star-forming regions with a wide range of brightness. The faintest region in the FUV has a brightness of 22.51 mag, while the brightest region has a brightness of 15.43 mag. Similarly, in the NUV band, the faintest and brightest star-forming regions have brightness values of 22.86 mag and 14.14 mag respectively. These star-forming regions have varied sizes, ranging from 0.008 to 0.242 kpc^2, with an average value of 0.020 kpc^2. We found $E(B - V)$ to vary from 0.04 to 1.17 mag, with an average value of 0.51 mag and a median of 0.49 mag. Extinction values in the FUV were found to lie between 0.19 and 5.34 mag, with an average of 2.33 mag and a median of 1.58 mag. In the NUV band, the extinction is lower, with values between 0.14 and 3.73 mag, with a median of 1.58 mag and an average of 1.63 mag.

Σ_{SFR} of these star-forming regions varied between 3.25×10^{-3} and $53.02 \times 10^{-2} M_\odot \, yr^{-1} \, kpc^{-2}$ in FUV and between 24.81×10^{-4} and $12.78 \times 10^{-2} M_\odot \, yr^{-1} \, kpc^{-2}$ in NUV. We found Σ_{SFR} to gradually decrease radially from the center to the outskirts, as can be seen in Figure 6.

5.7. NGC 6814

NGC 6814 is a grand design spiral galaxy of the SAB(rs)bc type, with a face-on orientation (de Vaucouleurs et al. 1991). It is characterized by a compact bulge in both near-infrared and optical wavelengths, along with a relatively weak bar extending approximately $10''$ in the north–south direction (Sánchez-Portal et al. 2004; Slavcheva-Mihova & Mihov 2011). Situated at a distance of 23.22 Mpc, this galaxy hosts a type 1.5 Seyfert AGN at its center (Springob et al. 2005), with a black hole of mass $(1.85 \pm 0.35) \times 10^7 M_\odot$ (Bentz et al. 2009). It is variable in the optical, UV, and X-ray wavelengths, with the greatest variability observed in X-rays (Troyer et al. 2016; Gallo et al. 2021). It is luminous in X-rays with $L_{2-10} = 2.04 \times 10^{42} \, erg \, s^{-1}$ (Tortosa et al. 2018). At radio frequencies, the central region appears extended in the north–south direction with a possible component toward the west, and no significant jet emission when observed with the VLA A-array, (Ulvestad & Wilson 1984; Xu et al. 1999).

Extensive work by Knapen et al. (1993) has identified numerous H II regions within the galaxy, with a comprehensive study of the luminosity functions of these regions. Interestingly, the luminosity function exhibits similar characteristics in both the outer and inner arms, offering valuable insights into the galaxy's SF processes. In addition to H II regions, NGC 6814 displays ringlike distributions of H II, potentially featuring kinematic warping, as suggested by Liszt & Dickey (1995). Moreover, in the UV spectrum, numerous star-forming regions are evident along the spiral arms, with these arms branching into multiple fragments observable in the GALEX images (Sandage & Bedke 1994).

We identified 89 star-forming regions in NGC 6814, with the faintest region at 21.21 mag and the brightest at 16.43 mag in the FUV band. These regions exhibited a range of sizes, with areas ranging from 0.029 to 0.422 kpc^2, with an average area of 0.118 kpc^2 and a median area of 0.082 kpc^2. The $E(B - V)$ values in the regions ranged from 0.15 to 0.59 mag, with an

average of 0.43 mag. Extinction in the FUV band was found to vary between 0.65 and 2.64 mag, with an average of 1.94 mag.

Σ_{SFR} of the star-forming regions identified in NGC 6814 showed variations, with the Σ_{SFR} values in the FUV band ranging from 8.96×10^{-3} to $65.25 \times 10^{-2} M_{\odot} \mathrm{yr}^{-1} \mathrm{kpc}^{-2}$, with an average of $4.19 \times 10^{-2} M_{\odot} \mathrm{yr}^{-1} \mathrm{kpc}^{-2}$. We found a gradual radial decrease of extinction and SFR from the center to the outskirts of the galaxy (see Figures 5 and 6).

5.8. NGC 7469

NGC 7469 is classified as an intermediate, nearly face-on spiral galaxy with a morphological type of (R')SAB(rs)a (de Vaucouleurs et al. 1991). This galaxy is located at a redshift of $z = 0.01627$ (Springob et al. 2005). It hosts a type 1.5 Seyfert AGN (Véron-Cetty & Véron 2006) with a black hole of mass $1.1 \times 10^{7} M_{\odot}$ (Peterson et al. 2014; Lu et al. 2021). It is known for its strong X-ray emission, with an X-ray luminosity of $L_{2-10\mathrm{keV}} = 10^{43}$ erg s^{-1} (Asmus et al. 2015).

One of the prominent features of this galaxy is its circumnuclear starburst ring, situated at a distance of about 1 kpc from its center. This starburst ring has been extensively observed across various wavelengths (Xu & Wang 2022). High-resolution radio continuum observations show a nucleus, which is the brightest feature, and more extended emission from the circumnuclear starburst with several peaks of emission. The brightest of the compact components is a radio supernova (Colina et al. 2001). Additionally, from observations of molecular line emission at millimeter wavelengths Davies et al. (2004) suggest the presence of either a bar or a pair of spiral arms located between these ringlike structures. Marquez & Moles (1994) suggest that the star-forming activities in this galaxy exhibit unique characteristics, potentially influenced by its Hα emission, which may be attributed to the nearby companion galaxy IC 5283.

In NGC 7469, we identified 26 star-forming regions. We detected more SF regions in the northern spiral arm, which may be due to the effect of interaction with nearby galaxy IC 5283 as mentioned by Marquez & Moles (1994). These regions in FUV have brightness ranging between 24.47 and 17.67 mag. In the NUV band, the faintest star-forming region is at 24.63 mag and the brightest is at 17.65 mag. Also, we found the areas of these star-forming regions to vary significantly, ranging from 0.295 to 63.642 kpc^2. On average, the star-forming regions have an average area of 12.026 kpc^2. $E(B - V)$ in these regions ranges from 0.06 to 0.64 mag. In the FUV band, we found extinction values that range from 0.27 to 2.68 mag, with an average of 1.17 mag. Similarly, in the NUV band, we found the extinction to vary from 0.22 to 2.21 mag, with a median of 0.97 mag.

Σ_{SFR} within these star-forming regions exhibits a wide range. In FUV, Σ_{SFR} varies from 8.0×10^{-4} to $49.39 \times 10^{-3} M_{\odot}$ yr^{-1} kpc^{-2}, with an average of $5.72 \times 10^{-3} M_{\odot} \mathrm{yr}^{-1} \mathrm{kpc}^{-2}$. In NUV, we found Σ_{SFR} to vary from 7.2×10^{-4} to $77.26 \times 10^{-3} M_{\odot} \mathrm{yr}^{-1} \mathrm{kpc}^{-2}$, with an average Σ_{SFR} of $7.08 \times 10^{-3} M_{\odot} \mathrm{yr}^{-1} \mathrm{kpc}^{-2}$.

6. Global Picture

For the galaxies examined in this study, we observed a positive correlation between the median surface density of SF and the extinction in the FUV band, with a Pearson correlation coefficient (r) of 0.95 and a p-value of 0.0003. This relationship
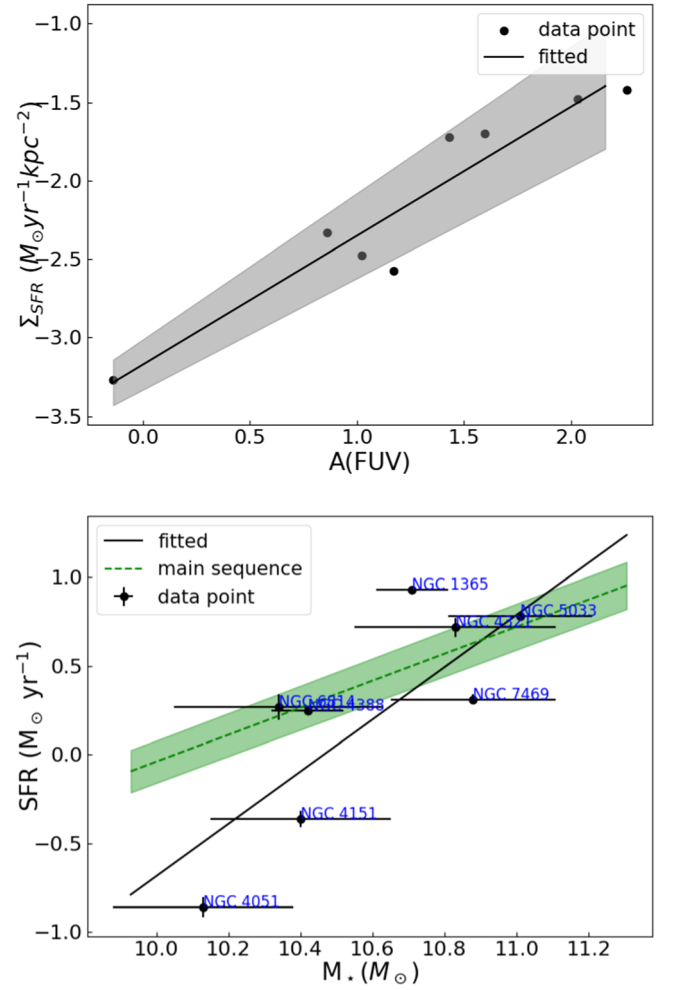

Figure 7. Top panel: variation of median Σ_{SFR} against median extinction in FUV of SF regions for the sources studied in this work. Bottom panel: variation of SFR with stellar mass. The dotted line is the MS of SF from Renzini & Peng (2015), and the solid line is the best-fitted linear regression line.

is illustrated in the top panel of Figure 7. The best-fitted line to this correlation is given by

$$\log \left(\frac{\Sigma_{\mathrm{SFR}}}{M_{\odot} \mathrm{yr}^{-1} \mathrm{kpc}^{-2}} \right) = (0.82 \pm 0.11) A(\mathrm{FUV}) - (3.17 \pm 0.16).$$

(5)

We determined the SFR using Equation (4a) within the circumnuclear region, employing a 1 kpc radius aperture, and computed the total SFR using the optical R_{25} aperture. In both cases, we corrected for AGN flux contamination using a $1''4$ radius aperture. Here, R_{25} represents the radius at which the surface brightness reaches 25 mag arcsec^{-2} in the optical B band. The results of these calculations are provided in Table 5. Additionally, detailed properties of each of the identified star-forming regions for all eight galaxies are presented in the Appendix.

We positioned our sources on the stellar mass versus SFR plane and compared their locations relative to the main sequence (MS) as described by Renzini & Peng (2015). Notably, four of our sources fell within the MS, one above it, and three below it. This distribution is illustrated in the bottom panel of Figure 7. The position of the AGN in M_{*}–SFR below the MS has also been noticed by Salim et al. (2007).

Table 5
Properties of the Galaxies in FUV

Name	SFR$_{Total}$	SFR$_{Nuclear}$	Σ_{SFR}^{Toal}	$\Sigma_{SFR}^{Nuclear}$
NGC 1365	8.469 ± 0.128	1.192 ± 0.019	2.83 ± 0.04	94.82 ± 1.62
NGC 4051	0.138 ± 0.008	0.050 ± 0.003	1.40 ± 0.08	15.82 ± 0.9
NGC 4151	0.434 ± 0.019	0.102 ± 0.004	1.48 ± 0.07	8.12 ± 0.41
NGC 4321	5.210 ± 0.281	0.617 ± 0.033	3.72 ± 0.21	48.11 ± 2.60
NGC 4388	0.32 ± 0.005	1.77 ± 0.02	3.22 ± 0.04	25.57 ± 0.4
NGC 5033	6.058 ± 0.0997	1.116 ± 0.024	10.34 ± 0.20	88.78 ± 1.91
NGC 6814	1.859 ± 0.134	0.351 ± 0.025	7.25 ± 0.52	27.90 ± 2.00
NGC 7469	2.042 ± 0.057	0.792 ± 0.030	4.25 ± 0.14	63.00 ± 2.41

Note. The units of SFR are $M_\odot$ yr^{-1}, while those of Σ_{SFR} are $10^{-3}\,M_\odot$ yr^{-1} kpc^{-2}.
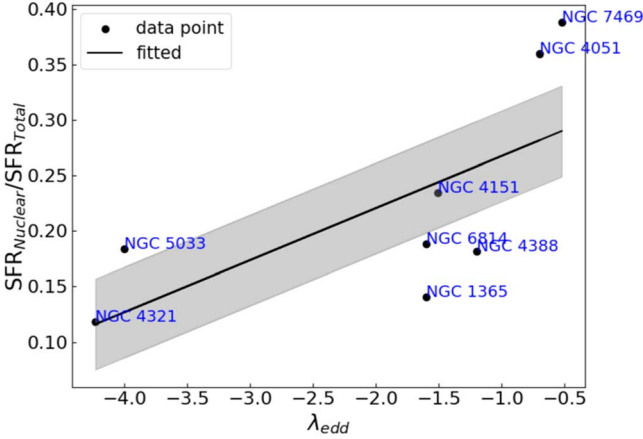
Figure 8. Variation of the ratio of SFR$_{Nuclear}$ to SFR$_{Total}$ with λ_{Edd}. The solid line is the linear least-squares fit to the data and the shaded region is the 95% confidence region.

Furthermore, we observed a positive correlation between the SFR and the stellar mass. Utilizing a linear regression analysis, we determined a correlation coefficient (r) of 0.83 and a p-value of 0.02. The resulting best-fitted line is represented by the equation

$$\log\left(\frac{\text{SFR}_{total}}{M_\odot\ \text{yr}^{-1}}\right) = (1.47 \pm 0.44)\log\left(\frac{M_\star}{M_\odot}\right) - (15.39 \pm 4.65). \quad (6)$$

We identified a modest positive correlation between the ratio of the nuclear SFR (SFR$_{Nuclear}$) to the total SFR (SFR$_{Total}$) and the Eddington ratio, λ_{Edd}. Here, λ_{Edd} represents the ratio of the bolometric luminosity (L_{Bol}) to the Eddington luminosity (L_{Edd}). To estimate L_{Bol}, we utilized the observed $L_{2-10\text{keV}}$ and applied the relation $\log(L_{Bol}) = 0.0378 \times \log(L_{2-10})^2 - 2.00 \times \log(L_{2-10}) + 60.5$ (Ichikawa et al. 2017), while L_{Edd} was calculated as $1.26 \times 10^{38}\,(M_{BH}/M_\odot)$ erg s^{-1}. This relationship is depicted in Figure 8. Performing a linear least-squares fit to the data points yielded a correlation coefficient (r) of 0.67 and a p-value of 0.06. The best-fitted line is

$$\frac{\text{SFR}_{Nuclear}}{\text{SFR}_{Total}} = (0.05 \pm 0.02)\log(\lambda_{Edd}) + (0.31 \pm 0.05). \quad (7)$$

This correlation bears resemblance to the findings of Mountrichas & Buat (2023) regarding the relationship between SFR and λ_{Edd}. However, we noted that this correlation is heavily influenced by two points, NGC 7469 and NGC 4051. Thus, further observations with more sources are required to confirm this correlation robustly. Nevertheless, the observed

correlation suggests that AGN activity (jet and/or radiation) positively influences the SF characteristics near the nuclear region, with minimal impact observed at greater distances from the nuclear region. However, disentangling the contributions of AGN jet and radiation is not possible using only the observations reported in this paper. Our observation aligns with both simulations (Bollati et al. 2023) and observational studies (Lammers et al. 2023), which support the operation of feedback processes primarily within the central kiloparsec region in AGN host galaxies.

7. Summary

We carried out an investigation of the SF characteristics of galaxies hosting AGN using observations carried out in the UV. Our sample consists of seven Seyfert-type and one LINER-type AGN. Our approach involved the identification of star-forming regions, carrying out aperture photometry of the identified star-forming regions, correcting the derived brightness for both Milky Way and internal extinction, estimation of SFR, and the correlation of SFR with various derived parameters. The findings of this work are summarized below.

1. We identified many star-forming regions for all eight galaxies hosting AGN. For NGC 5033, we detected the maximum number of SF regions. Most of the identified star-forming regions have sizes in excess of 30 pc, with areas ranging between 0.010 and 63.642 kpc^2.

2. The extinction-corrected SFR of the star-forming regions considering all the sources studied in this work is found to range between 1.09×10^{-4} and $22.96 \times 10^{-2}\,M_\odot$ yr^{-1} in FUV, while in NUV it varies between 8.15×10^{-5} and $6.634\,M_\odot$ yr^{-1}. We found Σ_{SFR} in NUV to be larger than that in FUV, though the median values are found to be similar.

3. We detected two outer spiral arms for NGC 4151 in both FUV and NUV bands. These spiral arms are much extended beyond the R_{25} aperture.

4. For five galaxies, NGC 1365, NGC 4051, NGC 4321, NGC 5033, and NGC 6814, we found both the internal extinction and Σ_{SFR} to gradually decrease from the center toward the outer regions, while this was not significant in the other sources.

5. We found a positive correlation between the median Σ_{SFR} and the median extinction in FUV for the star-forming regions.

6. Among the observed sources, four are situated within the MS of star-forming galaxies, while the remaining four are positioned away from the MS.

7. All sources display a positive correlation between SFR and M_*, with a slope that is notably steeper than the MS.

8. We found the SFR in the nuclear region to be dominant over the total SFR.

9. The ratio of $SFR_{Nuclear}$ to SFR_{Total} exhibits a weak positive correlation with λ_{Edd}. This correlation points to the influence of AGN in enhancing the SF characteristics of the hosts and to the impact being dominant in the central region with no effect on scales beyond the nuclear region probed in this work.

Appendix
Some Extra Material

Properties of the identified star-forming regions are provided in Table 6.

Table 6
Properties of the Identified Star-forming Regions for the Galaxies in our Sample

Host Galaxy Name	R.A.	Decl.	a	b	θ	r_d	Area	$E(B-V)$	$m_{\rm FUV}$	$m_{\rm NUV}$	$A_{\rm FUV}$	$A_{\rm NUV}$	$\Sigma_{\rm FUV}$	$\Sigma_{\rm NUV}$
NGC 1365	03:33:26.07	−36:12:49.39	5.58	3.45	0.009	36.26	0.936	0.102	17.97 ± 0.08	18.18 ± 0.07	0.44	0.33	13.82 ± 0.46	12.0 ± 0.32
NGC 1365	03:33:26.09	−36:12:44.44	5.16	2.59	0.769	35.69	0.651	0.109	18.55 ± 0.1	18.74 ± 0.08	0.48	0.35	11.75 ± 0.49	10.32 ± 0.35
NGC 1365	03:33:26.02	−36:12:54.31	2.65	2.13	1.504	36.84	0.275	0.112	19.57 ± 0.16	19.76 ± 0.13	0.49	0.36	10.8 ± 0.7	9.54 ± 0.51
NGC 1365	03:33:25.51	−36:12:41.75	3.76	1.66	0.79	35.79	0.303	0.088	19.73 ± 0.17	19.95 ± 0.14	0.38	0.28	8.5 ± 0.57	7.24 ± 0.4
NGC 1365	03:33:24.70	−36:12:53.92	4.03	2.49	0.291	37.7	0.489	0.091	19.39 ± 0.14	19.61 ± 0.12	0.4	0.29	7.16 ± 0.42	6.12 ± 0.3
NGC 1365	03:33:24.81	−36:12:50.19	3.12	2.23	−0.497	37.21	0.338	0.102	19.77 ± 0.17	19.98 ± 0.14	0.45	0.33	7.3 ± 0.51	6.34 ± 0.36
NGC 1365	03:33:25.11	−36:12:43.54	4.24	2.51	0.774	36.27	0.519	0.111	19.5 ± 0.16	19.68 ± 0.13	0.49	0.36	6.15 ± 0.38	5.42 ± 0.28
NGC 1365	03:33:24.33	−36:12:58.13	4.89	2.59	−0.051	38.42	0.614	0.097	19.84 ± 0.18	20.05 ± 0.15	0.42	0.31	3.79 ± 0.27	3.27 ± 0.19
NGC 1365	03:33:23.91	−36:12:55.71	3.86	2.11	−1.316	38.46	0.396	0.118	20.43 ± 0.24	20.61 ± 0.2	0.52	0.38	3.39 ± 0.32	3.02 ± 0.24
NGC 1365	03:33:27.23	−36:12:48.16	6.02	4.37	0.492	35.39	1.278	0.183	19.32 ± 0.16	19.39 ± 0.13	0.8	0.59	2.94 ± 0.18	2.89 ± 0.15

Note. Here, a, b, and θ are the semimajor axis, semiminor axis, and the position angle of the star-forming regions, area is the area of the regions in kpc^2, $E(B-V)$ is the color excess in magnitudes, $m_{\rm FUV}$ and $m_{\rm NUV}$ are the magnitudes of the FUV and NUV bands, $A_{\rm FUV}$ and $A_{\rm NUV}$ are the extinctions in FUV and NUV bands, and $\Sigma_{\rm FUV}$ and $\Sigma_{\rm NUV}$ are the surface densities of SFR in units of $10^{-3}\,M_\odot\,{\rm yr}^{-1}\,{\rm kpc}^{-2}$ in FUV and NUV bands respectively.

(This table is available in its entirety in machine-readable form in the online article.)

ORCID iDs

Payel Nandi ● https://orcid.org/0009-0003-9765-3517
C. S. Stalin ● https://orcid.org/0000-0002-4998-1861
Poulomi Dam ● https://orcid.org/0009-0007-7842-9930
D. J. Saikia ● https://orcid.org/0000-0002-4464-8023

References

Agrawal, P. C. 2006, AdSpR, 38, 2989
Allison, J. R., Sadler, E. M., & Meekin, A. M. 2014, MNRAS, 440, 696
Álvarez-Álvarez, M., Díaz, A. I., Terlevich, E., & Terlevich, R. 2015, MNRAS, 451, 3173
Andreani, P., Boselli, A., Ciesla, L., et al. 2018, A&A, 617, A33
Arsenault, R. 1989, A&A, 217, 66
Asmus, D., Gandhi, P., Hönig, S. F., Smette, A., & Duschl, W. J. 2015, MNRAS, 454, 766
Bentz, M. C., Denney, K. D., Cackett, E. M., et al. 2006, ApJ, 651, 775
Bentz, M. C., & Manne-Nicholas, E. 2018, ApJ, 864, 146
Bentz, M. C., Walsh, J. L., Barth, A. J., et al. 2009, ApJ, 705, 199
Bertin, E., & Arnouts, S. 1996, A&AS, 117, 393
Bing, L., Shi, Y., Chen, Y., et al. 2019, MNRAS, 482, 194
Bollati, F., Lupi, A., Dotti, M., & Haardt, F. 2023, arXiv:2311.07576
Bosma, A., Ekers, R. D., & Lequeux, J. 1977, A&A, 57, 97
Bradley, L., Sipőcz, B., Robitaille, T., et al. 2020, astropy/photutils: v1.0.0, Zenodo, doi:10.5281/zenodo.4044744
Brenneman, L. W., Risaliti, G., Elvis, M., & Nardini, E. 2013, MNRAS, 429, 2662
Byrne, L., Faucher-Giguère, C.-A., Wellons, S., et al. 2023, arXiv:2310.16086
Calzetti, D., Armus, L., Bohlin, R. C., et al. 2000, ApJ, 533, 682
Cardelli, J. A., Clayton, G. C., & Mathis, J. S. 1989, ApJ, 345, 245
Cayatte, V., van Gorkom, J. H., Balkowski, C., & Kotanyi, C. 1990, AJ, 100, 604
Cid Fernandes, R., Gu, Q., Melnick, J., et al. 2004, MNRAS, 355, 273
Colina, L., Alberdi, A., Torrelles, J. M., Panagia, N., & Wilson, A. S. 2001, ApJL, 553, L19
Couto, G. S., & Storchi-Bergmann, T. 2023, Galax, 11, 47
Damas-Segovia, A., Beck, R., Vollmer, B., et al. 2016, ApJ, 824, 30
Davies, R. I., Müller Sánchez, F., Genzel, R., et al. 2007, ApJ, 671, 1388
Davies, R. I., Sugai, H., & Ward, M. J. 1998, MNRAS, 300, 388
Davies, R. I., Tacconi, L. J., & Genzel, R. 2004, ApJ, 602, 148
de Vaucouleurs, G., de Vaucouleurs, A., Corwin, H. G. J., et al. 1991, Third Reference Catalogue of Bright Galaxies (New York: Springer)
Diniz, M. R., Riffel, R. A., Storchi-Bergmann, T., & Riffel, R. 2019, MNRAS, 487, 3958
Evans, I. N., Koratkar, A. P., Storchi-Bergmann, T., et al. 1996, ApJS, 105, 93
Falcke, H., Wilson, A. S., & Simpson, C. 1998, ApJ, 502, 199
Ferrarese, L., & Merritt, D. 2000, ApJL, 539, L9
Ferreras, I., Cropper, M., Kawata, D., Page, M., & Hoversten, E. A. 2012, MNRAS, 424, 1636
Fiore, F., Feruglio, C., Shankar, F., et al. 2017, A&A, 601, A143
Forster, K., Leighly, K. M., & Kay, L. E. 1999, ApJ, 523, 521
Gaia Collaboration, Vallenari, A., Brown, A. G. A., et al. 2023, A&A, 674, A1
Gallagher, R., Maiolino, R., Belfiore, F., et al. 2019, MNRAS, 485, 3409
Gallo, L. C., Gonzalez, A. G., & Miller, J. M. 2021, ApJL, 908, L33
García-Bernete, I., Alonso-Herrero, A., García-Burillo, S., et al. 2021, A&A, 645, A21
Garcia-Burillo, S., Sempere, M. J., Combes, F., & Neri, R. 1998, A&A, 333, 864
García-González, J., Alonso-Herrero, A., Hernán-Caballero, A., et al. 2016, MNRAS, 458, 4512
Gebhardt, K., Bender, R., Bower, G., et al. 2000, ApJL, 539, L13
Georgiev, I. Y., Böker, T., Leigh, N., Lützgendorf, N., & Neumayer, N. 2016, MNRAS, 457, 2122
Ghosh, S. K., Tandon, S. N., Singh, S. K., et al. 2022, JApA, 43, 77
González-Martín, O., Masegosa, J., Márquez, I., Guainazzi, M., & Jiménez-Bailón, E. 2009, A&A, 506, 1107
Gu, Q., Dultzin-Hacyan, D., & de Diego, J. A. 2001, RMxAA, 37, 3
Häring, N., & Rix, H.-W. 2004, ApJL, 604, L89
Harrison, C. M. 2017, NatAs, 1, 0165
Hennig, M. G., Riffel, R. A., Dors, O. L., et al. 2018, MNRAS, 477, 1086
Hervella Seoane, K., Ramos Almeida, C., Acosta Pulido, J. A., et al. 2023, A&A, 680, A71
Hummel, E., & Saikia, D. J. 1991, A&A, 249, 43
Ichikawa, K., Ricci, C., Ueda, Y., et al. 2017, ApJ, 835, 74

Immler, S., Pietsch, W., & Aschenbach, B. 1998, A&A, 331, 601
Jones, S., McHardy, I., Moss, D., et al. 2011, MNRAS, 412, 2641
Kennicutt, R. C., & Evans, N. J. 2012, ARA&A, 50, 531
Khachikian, E. Y., & Weedman, D. W. 1974, ApJ, 192, 581
Knapen, J. H., Arnth-Jensen, N., Cepa, J., & Beckman, J. E. 1993, AJ, 106, 56
Kumari, N., Jana, A., Naik, S., & Nandi, P. 2023, MNRAS, 521, 5440
Kuo, C. Y., Braatz, J. A., Condon, J. J., et al. 2011, ApJ, 727, 20
Lammers, C., Iyer, K. G., Ibarra-Medel, H., et al. 2023, ApJ, 953, 26
Liszt, H. S., & Dickey, J. M. 1995, AJ, 110, 998
Lu, K.-X., Wang, J.-G., Zhang, Z.-X., et al. 2021, ApJ, 918, 50
Lu, N. Y., Hoffman, G. L., Groff, T., Roos, T., & Lamphier, C. 1993, ApJS, 88, 383
Maiolino, R., & Rieke, G. H. 1995, ApJ, 454, 95
Maiolino, R., Russell, H. R., Fabian, A. C., et al. 2017, Natur, 544, 202
Marconi, A., & Hunt, L. K. 2003, ApJL, 589, L21
Marquez, I., & Moles, M. 1994, AJ, 108, 90
Martin, D. C., Fanson, J., Schiminovich, D., et al. 2005, ApJL, 619, L1
McHardy, I. M., Papadakis, I. E., Uttley, P., Page, M. J., & Mason, K. O. 2004, MNRAS, 348, 783
McLure, R. J., & Dunlop, J. S. 2002, MNRAS, 331, 795
Mountrichas, G., & Buat, V. 2023, A&A, 679, A151
Mundell, C. G., Pedlar, A., Shone, D. L., & Robinson, A. 1999, MNRAS, 304, 481
Nandi, P., Stalin, C. S., Saikia, D. J., et al. 2023a, ApJ, 950, 81
Nandi, P., Stalin, C. S., Saikia, D. J., et al. 2023b, ApJ, 959, 116
Pan, H.-A., & Kuno, N. 2017, ApJ, 839, 133
Papadakis, I. E., Ioannou, Z., Brinkmann, W., & Xilouris, E. M. 2008, A&A, 490, 995
Parkash, V., Brown, M. J. I., Jarrett, T. H., & Bonne, N. J. 2018, ApJ, 864, 40
Paturel, G., Petit, C., Prugniel, P., et al. 2003, A&A, 412, 45
Pedlar, A., Howley, P., Axon, D. J., & Unger, S. W. 1992, MNRAS, 259, 369
Pérez-Torres, M. A., & Alberdi, A. 2007, MNRAS, 379, 275
Peterson, B. M., Grier, C. J., Horne, K., et al. 2014, ApJ, 795, 149
Peterson, B. M., McHardy, I. M., Wilkes, B. J., et al. 2000, ApJ, 542, 161
Pounds, K. A., Reeves, J. N., King, A. R., & Page, K. L. 2004, MNRAS, 350, 10
Renzini, A., & Peng, Y.-j. 2015, ApJL, 801, L29
Riffel, R., Dahmer-Hahn, L. G., Riffel, R. A., et al. 2022, MNRAS, 512, 3906
Risaliti, G., Elvis, M., Fabbiano, G., Baldi, A., & Zezas, A. 2005, ApJL, 623, L93
Risaliti, G., Miniutti, G., Elvis, M., et al. 2009, ApJ, 696, 160
Rodriguez Espinosa, J. M., Rudy, R. J., & Jones, B. 1987, ApJ, 312, 555
Saikia, D. J., Pedlar, A., Unger, S. W., & Axon, D. J. 1994, MNRAS, 270, 46
Salim, S., Rich, R. M., Charlot, S., et al. 2007, ApJS, 173, 267
Sánchez-Portal, M., Díaz, Á., Terlevich, E., & Terlevich, R. 2004, MNRAS, 350, 1087
Sandage, A., & Bedke, J. 1994, The Carnegie Atlas of Galaxies (Washington, DC: Carnegie Institution of Washington)
Sandqvist, A., Joersaeter, S., & Lindblad, P. O. 1995, A&A, 295, 585
Sargent, A. J., Fischer, T. C., Johnson, M. C., et al. 2024, ApJ, 961, 230
Sarzi, M., Rix, H.-W., Shields, J. C., et al. 2002, ApJ, 567, 237
Seifina, E., Chekhtman, A., & Titarchuk, L. 2018, A&A, 613, A48
Shin, J., Woo, J.-H., Chung, A., et al. 2019, ApJ, 881, 147
Singh, A., Gulati, M., & Bagla, J. S. 2019, MNRAS, 489, 5582
Slavcheva-Mihova, L., & Mihov, B. 2011, A&A, 526, A43
Springob, C. M., Haynes, M. P., Giovanelli, R., & Kent, B. R. 2005, ApJS, 160, 149
Stevens, I. R., Forbes, D. A., & Norris, R. P. 1999, MNRAS, 306, 479
Storchi-Bergmann, T., & Schnorr-Müller, A. 2019, NatAs, 3, 48
Sweet, S. M., Fisher, D., Glazebrook, K., et al. 2018, ApJ, 860, 37
Tandon, S. N., Postma, J., Joseph, P., et al. 2020, AJ, 159, 158
Terashima, Y., Kunieda, H., & Misaki, K. 1999, PASJ, 51, 277
Tody, D. 1986, Proc. SPIE, 627, 733
Tortosa, A., Bianchi, S., Marinucci, A., et al. 2018, MNRAS, 473, 3104
Troyer, J., Starkey, D., Cackett, E. M., et al. 2016, MNRAS, 456, 4040
Tsai, M., & Hwang, C.-Y. 2015, AJ, 150, 43
Tueller, J., Mushotzky, R. F., Barthelmy, S., et al. 2008, ApJ, 681, 113
Ulvestad, J. S., & Wilson, A. S. 1984, ApJ, 285, 439
Urbanik, M., Klein, U., & Graeve, R. 1986, A&A, 166, 107
Veilleux, S., Bland-Hawthorn, J., & Cecil, G. 1999, AJ, 118, 2108
Véron-Cetty, M. P., & Véron, P. 2006, A&A, 455, 773
Wang, J., Risaliti, G., Fabbiano, G., et al. 2010, ApJ, 714, 1497
Ward, S. R., Harrison, C. M., Costa, T., & Mainieri, V. 2022, MNRAS, 514, 2936
Weiler, K. W., van der Hulst, J. M., Sramek, R. A., & Panagia, N. 1981, ApJL, 243, L151

Whitmore, B. C., Chandar, R., Rodríguez, M. J., et al. 2023, ApJL, 944, L14
Williams, D. R. A., McHardy, I. M., Baldi, R. D., et al. 2017, MNRAS, 472, 3842
Wolfinger, K., Kilborn, V. A., Koribalski, B. S., et al. 2013, MNRAS, 428, 1790
Xu, C., Livio, M., & Baum, S. 1999, AJ, 118, 1169
Xu, X., & Wang, J. 2022, ApJ, 933, 110
Yang, T., Davé, R., Cui, W., et al. 2024, MNRAS, 527, 1612
Zhang, L., & Ho, L. C. 2023, ApJL, 953, L9
Zhuang, M.-Y., Ho, L. C., & Shangguan, J. 2021, ApJ, 906, 38
Zinn, P. C., Middelberg, E., Norris, R. P., & Dettmar, R. J. 2013, ApJ, 774, 66